International Journal of Rock Mechanics & Mining Sciences 134 (2020) 104442

Contents lists available at ScienceDirect

International Journal of Rock Mechanics and Mining Sciences

journal homepage: http://www.elsevier.com/locate/ijrmms

Mineralogical characterization and macro/microstrain analysis of the Marcellus shales

Gunes A. Yakaboylu [a], Neel Gupta [b], Edward M. Sabolsky [a], Brijes Mishra [b,*]

[a] Department of Mechanical and Aerospace Engineering, West Virginia University, Morgantown, WV, USA
[b] Department of Mining Engineering, West Virginia University, Morgantown, WV, USA

ARTICLE INFO

Keywords
Marcellus shale
Microcracking
Strain analysis
Creep
Calcite
Deformation

ABSTRACT

Due to the complex structure of the brittle formations like shale, their microcracking and mechanical deformation behavior are not well known. To understand the fundamental factors at the micron scale, Marcellus shales were cored both parallel and perpendicular to the bedding orientation and mechanically tested through triaxial creep test under constant stress. The parallel-bedded shales exhibited higher level of permanent strain in the radial direction, which increased with increasing time. This also confirmed their anisotropic nature due to the bedding. Their advanced characterization via X-ray diffraction (XRD) and Raman spectroscopy techniques before and after the creep tests revealed the mineralogical heterogeneity, and the presence of an organic matter (kerogen) concentrated in the microcrack areas. Besides, the XRD peak shifts and changes in peak shape indicated that there was a certain level of macrostrain and microstrain in the shale. Further investigation of the XRD peak shape (integral breadth) changes using the Williamson-Hall method demonstrated a higher concentration of lattice defects and associated microstrain (inhomogeneous lattice strain) present in the calcite phase compared to the quartz. The parallel-bedded shales also revealed a higher level of microstrain with respect to the perpendicular-bedding. The results proved that the microcracking (initiation and propagation) and associated mechanical deformation of the Marcellus shales were mostly influenced by the presence of organic matter, microstrain level (defect concentration) in the calcite mineral, and the bedding orientation.

1. Introduction

In underground coal mines, the stresses induced by coal excavation deform the surrounding rock mass, such that the permanently supported or unsupported mine entries undergo an unexpected failure.[1] In the Appalachian Basin, shale is known to be the most common immediate roof to the Pittsburgh coal seam.[2] With the numerous thin bedding planes or laminations, shale is an anisotropic rock with smaller strength in the direction of bedding planes.[3] It is moisture sensitive and a weak rock mass,[4] which also exhibits time-dependent deformation under a constant stress state.[5] The various empirical and numerical modelling studies proved that the level of constant stress, moisture content, temperature, mineralogical composition, and anisotropy significantly influence the creep deformation in shale.[6,7] Since the failure of the permanently supported shale roofs leads to the mine fatality or closure of mine entries, it is highly necessary to investigate the fundamental reasons behind the time-dependent deformation or creep in shale for a better mechanistic understanding.

The small scale microcracking was recently determined to be the main reason of the creep failure in the Marcellus shale,[1] as similar to the other types of brittle rocks, such as, quartz and granite.[8] Conventionally, the microcracks can grow when either the local stress at the tip of the microcrack increases or the strength of the tip of the microcrack decreases.[8] In the case of the constant strain rate experiments, the continuous increase in the far-field compressive stresses increases the local stresses at the microcrack tip, and therefore, these microcracks typically grow in the direction of the maximum compressive stress. However, in the creep experiments, the constant nature of far-field compressive stresses does not change the local stresses at the microcrack tip, and thereby, the microcrack growth occurs mainly due to the decrease in the strength of the microcrack tip. Furthermore, corrosive agents, such as moisture, temperature and interaction between cavities,

DOI of original article: https://doi.org/10.1016/j.ijrmms.2020.104345.
* Corresponding author. Department of Mining Engineering, West Virginia University, 1374 Evansdale Drive, Morgantown, WV, 26506, USA.
E-mail addresses: gayakaboylu@mix.wvu.edu (G.A. Yakaboylu), negupta@mix.wvu.edu (N. Gupta), ed.sabolsky@mail.wvu.edu (E.M. Sabolsky), brijes.mishra@mail.wvu.edu (B. Mishra).

https://doi.org/10.1016/j.ijrmms.2020.104442

Available online 15 August 2020

may also reduce the microcrack tip strength.[9] Therefore, the stress corrosion in the presence of water or moisture is the primary reason of sub-critical growth of such microcracks at constant stress state for the brittle rocks (e.g. quartz). However, due to the significant changes in the mineralogy, mechanical properties, pore structure and anisotropy of different brittle rocks like shale,[10] it should be noted that the fundamental reason of microcracking in shale at constant stress is not well understood, and cannot be explained only by the described stress corrosion mechanism itself.

Based on these facts, further studies and utilization of the advanced characterization techniques can provide new insights and further fundamental understanding on the microcracking and deformation behavior in shale. Therefore, we used bedded Marcellus shale specimens, which were cored parallel (PL) and perpendicular (PD) to the orientation of bedding planes. The triaxial creep tests measured the permanent macrostrain in the shale specimens. Although the macrostrain referring to average uniform strain value over a macroscopic region is essential; the microcracking, deformation behavior and mechanical performance of the brittle rocks are mostly controlled by the defects and the associated microstrains.[11] However, the microstrain aspect of their deformation has not been addressed yet. To provide a mechanistic understanding at the micron-scale, the as-cut samples from bottom and top regions of the Marcellus shale specimens were characterized by the X-ray diffraction (XRD) and the Raman spectroscopy, following the triaxial creep tests. These techniques can be efficiently applied for the bulk and local mineral identification, as well as, the detection of the presence of an organic matter.[12,13] In recent years, they are considered as indispensable tools for the characterization of various rocks and minerals, such as, phosphorite, shale, granite, and quartz.[14–16] In addition to the chemical analysis, the changes in the XRD peak profiles (termed as peak or line broadening) can be further evaluated to estimate the lattice strain or microstrain directly caused by the presence of defects (e.g. point defects, dislocations).[17–19] Among the various techniques (e.g. Warren-Averbach analysis, Rietveld refinement), the Williamson-Hall method[20] was applied in this study for the estimation of the microstrain in the Marcellus shale specimens. Therefore, in brief, the main objective of this study was to understand the factors influencing the microcracking and mechanical deformation in Marcellus shale over a microscopic scale by utilizing mechanical, bulk/local mineral or chemical, and microstrain analysis techniques.

2. Materials and methods

2.1. Marcellus shale specimens

The shale specimens were retrieved from an outcrop of Marcellus formation located in the western New York. Marcellus shale is an organic rich shale formation, extends in the subsurface from New York state in the north to the northeastern Kentucky and Tennessee in the south, eastern Ohio to extreme western Virginia.[21] Marcellus shale primarily contains carbonaceous silty black shale with scattered pyrite, scarce fossils and carbonate concretions. Its color ranges from medium light gray to black, which provides information about the depositional environment. For example, the shale deposited in the oxygen-deficient environment is typically black in color with high organic content. The Marcellus shale specimens used in this study were light gray in color, cored both parallel (PL) and perpendicular (PD) to the orientation of bedding planes. It should be noted that, for simplicity, the parallel- and perpendicular-bedded shale specimens were abbreviated as PL and PD, respectively. Each specimen was cylindrical shaped with both ends polished and ground flat to maintain the ends parallel to 0.0013 mm. The diameter and length of all shale specimens were 2.1 and 4.2 inches (or 53.4 and 106.8 mm), respectively.

2.2. Triaxial creep tests on cylindrical shale specimens

The constant load values for the triaxial creep tests were determined based on the triaxial strength of the Marcellus shales at similar confining stress state. In these tests, the confining stress remained constant, and axial stress was controlled by constant strain rate of 0.001% per second. The average triaxial strength of parallel-bedded shale specimens (142.7 MPa) was measured to be higher than the perpendicular-bedded ones (132.2 MPa), indicating the anisotropic nature of the Marcellus shales, as reported in our previous study.[1] In this study, six Marcellus shale specimens including three perpendicular (PD) and three parallel (PL) bedded were tested under constant triaxial stress state for different time intervals. The ratio of the specimen length to diameter was 2:1 for each specimen, which is suitable for the standardized testing of the intact rock core specimens.[22] The servo-controlled triaxial rock testing system (RTX-1500, GCTS Testing Systems, Tempe AZ, USA) was used to apply the conventional triaxial stress to the cylindrical shale specimens, such that the major principal stress (σ_1) > intermediate (σ_2) = minor principal stress (σ_3). The specimen in the triaxial cell was mounted with the axial and radial linear variable differential transformers (LVDTs) for accurate measurement of the strain in axial and radial directions. The level of the constant triaxial stress was measured from the short-term triaxial strength of the shale specimens, such that, for both types of bedded specimens, the constant stress was equivalent to 70% of the failure strength at the confining pressure of 6.89 MPa.[1] After the completion of the triaxial creep tests and the complete removal of the applied load, the permanent strain within the shale specimens was recorded by the onboard axial and radial LVDTs.

2.3. Specimen preparation protocol for materials characterization

Following the triaxial creep tests, the specific locations of the large shale specimens, where the stress-induced microcracks are mostly populated, were determined both at their top (T) and bottom (B) sides. The baseline data was created for the unstressed shale specimens using similar identification of the pre-existing microcrack populated regions. For simplicity, the as-cut shale specimens were designated based on the bedding plane orientation, sample number and cut region. As an example, the *PD-1 (T)* refers to the top-side cut of a perpendicular-bedded Marcellus shale specimen after the creep test, while the *PL-Unstressed (B)* corresponds to the bottom-side cut of a parallel-bedded Marcellus shale specimen before the creep test. These specific cut locations from the top and bottom side of the shale specimens along with the sample identifications are listed in Table 1.

In order to preserve the pre-existing and stress-induced microcracks

Table 1
Marcellus shale specimen identifications and top/bottom-side specific cut locations.

Specimen ID before cutting	Cut Locations (mm)		Specimen ID after cutting
	Top-side (T)	Bottom-side (B)	
PD-Unstressed	13.8	11.8	• PD-Unstressed (T) • PD-Unstressed (B)
PD-1	12.6	12.1	• PD-1 (T) • PD-1 (B)
PD-2	13.8	14.0	• PD-2 (T) • PD-2 (B)
PD-3	8.4	–	• PD-3 (T)
PL-Unstressed	14.5	13.5	• PL-Unstressed (T) • PL-Unstressed (B)
PL-1	17.0	9.5	• PL-1 (T) • PL-1 (B)
PL-2	21.0	15.2	• PL-2 (T) • PL-2 (B)
PL-3	27.0	15.0	• PL-3 (T) • PL-3 (B)

for the following materials characterization studies, a specimen preparation protocol was developed specifically for the shale and similar specimens. The flowchart of the developed protocol and the optical images of the representative shale specimens recorded at different stages are presented in Fig. 1. A high-viscosity epoxy gel (Devcon, ITW Polymers Adhesives, Danvers MA, USA) was initially applied to the surface of the Marcellus shale specimens. The applied epoxy was then cured for 18–24 h at room temperature. This was followed by dry cutting of the shale specimens from the epoxy applied regions using a 10 inch diameter diamond blade in a tile saw (MK-100, MK Diamond Products, Torrance CA, USA). Due to their potential moisture sensitivity, the dry cutting process was preferred to preserve the mineralogical composition without creating any external damage prior to the materials characterization. The rough surface of the shale specimens after the dry cutting process was evident as shown in Fig. 1. Therefore, the as-cut shale specimens were dry polished using 600 and 1200 grits of silicon carbide (SiC) polishing sheets for nearly 10 and 5 min, respectively. This was followed by fast cleaning of the as-polished specimen surfaces using 200-proof (anhydrous) ethanol. As presented in the optical image of a representative shale specimen prepared via the developed protocol, the existing microcracks and non-crack areas can be easily located. This is highly beneficial for the following mineral identification and microstrain analysis from both bulk and surface (local regions) of the shale specimens.

2.4. Materials characterization and microstrain analysis

The as-prepared Marcellus shale specimens were characterized by X-ray diffraction (XRD, Panalytical X'Pert Pro diffractometer, Westborough MA, USA) in a continuous scan mode over the 2θ range of 20°–70° with CuK_α radiation ($\lambda = 1.5406$ Å). For all XRD line profile data, a X-ray source at 45 kV and 40 mA was utilized under a slow scanning rate (1°/min) and a step size of 0.004°. In addition to the bulk characterization by XRD, the microcracks and non-crack areas were locally analyzed by a Raman spectrometer (Renishaw InVia Raman, New Mills, UK) using the 532 nm Ar laser as an excitation source. In addition, the standard calcite ($CaCO_3$, anhydrous, reagent grade, 98%, VWR, Radnor PA, USA) and quartz (SiO_2, fine-granular for analysis, washed and calcinated, MilliporeSigma, Danvers MA, USA) powders were analyzed under the same conditions to create a baseline data. Prior to the collection of the Raman spectra of the Marcellus shale specimens, the spectrometer was calibrated using a Si standard sample based on the characteristic Si band position at 521 cm^{-1}. The Raman spectra for each shale specimen were collected from one microcrack area and one non-crack area over the range of 100–2000 cm^{-1} using a 50 × objective lens. The laser power and acquisition time were 10% and 10 seconds, respectively. Three accumulations were combined for achieving each spectrum.

Following the mineral identification, the Williamson-Hall method was applied to the XRD line profile data in order to estimate the residual non-uniform (inhomogeneous) microstrain within each Marcellus shale

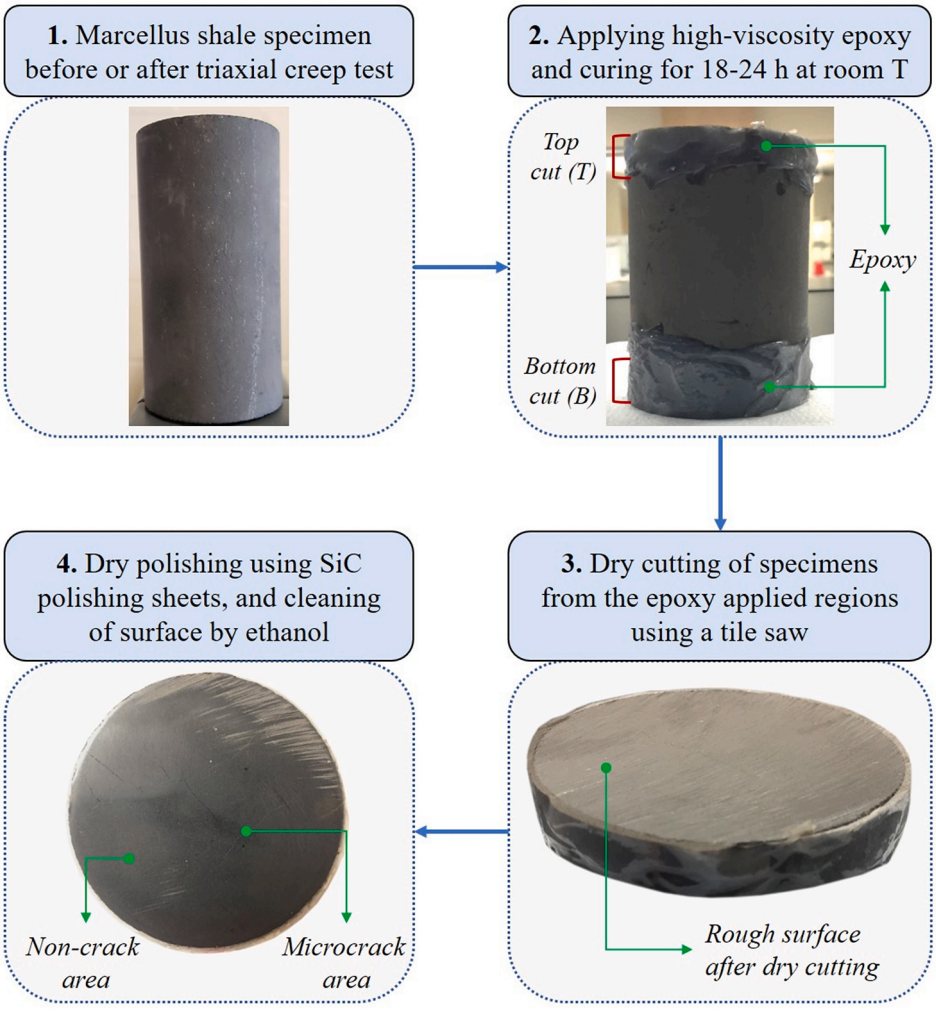

Fig. 1. Flowchart of the developed specimen preparation protocol and example optical images of the Marcellus shale specimens at different stages.

specimen.[20,23] The microstrain is local and non-uniform strain on a microscopic level, which typically consists of two components as (1) the average strain over a single grain, and (2) the strain fluctuation inside a grain.[24,25] The microstrain analyses were carried out individually for the major calcite and quartz phases due to the multiphase shale system. Due to the large grain size of the minerals within the shale specimens, it is assumed that the effects due to grain size broadening is negligible. Furthermore, it is known that the XRD line profiles (peak broadening) are affected by the instrumental broadening factor. Therefore, a standard potassium chloride (KCl, 99% min., Fisher Scientific, Waltham MA, USA) powder was additionally analyzed under the same XRD conditions to determine the integral breadth (*peak area divided by peak height*) caused by instrumental broadening.[26] The instrumental integral breadth (β_{ins}) was measured to be 2.168×10^{-3} radian (or 0.1242°) for the (200) reflection at $2\theta = 28.3°$. Following this, the experimental integral breadths, that were only related to the microstrain broadening (β), were

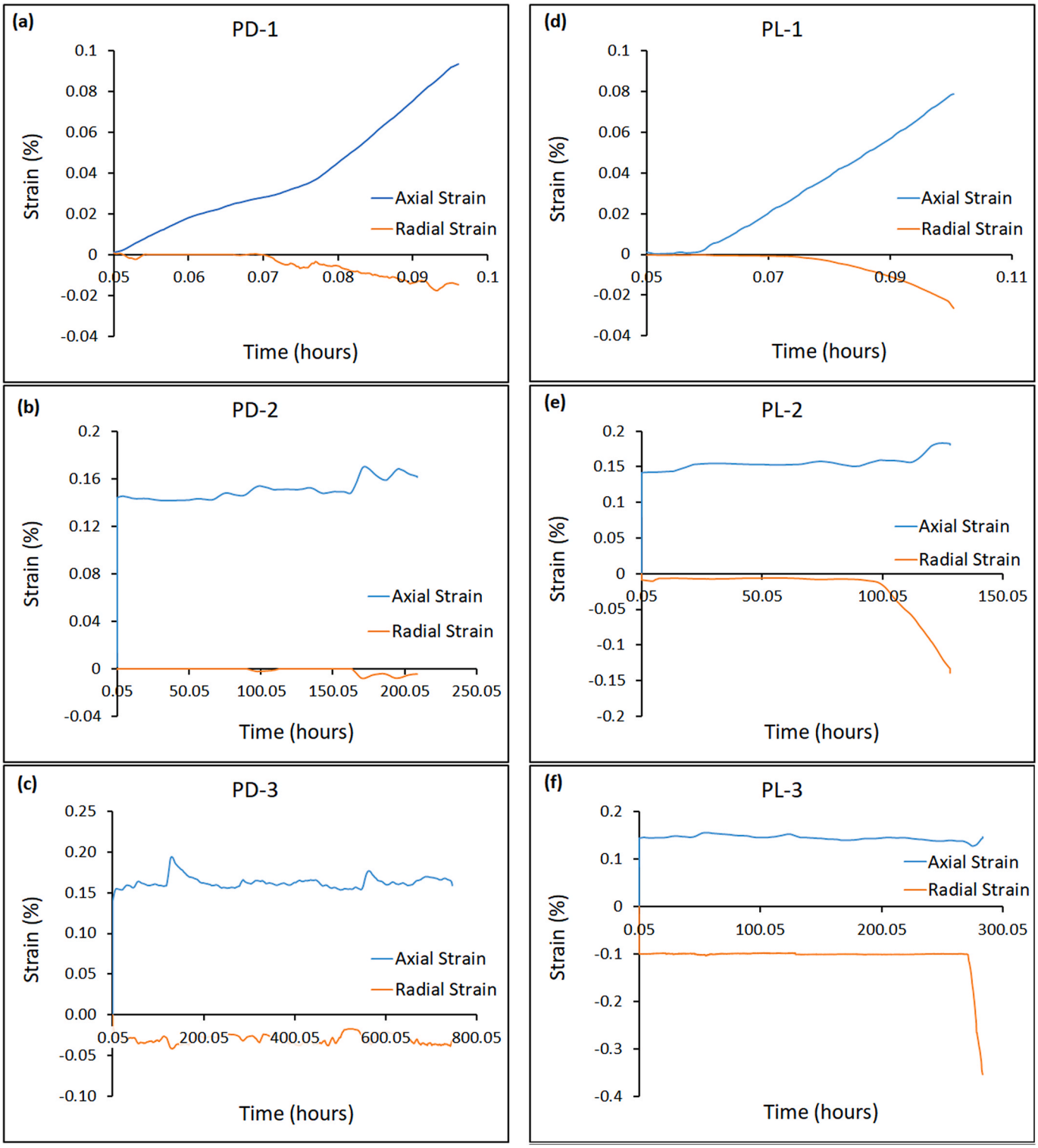

Fig. 2. Strain-time curves for the perpendicular (PD) and parallel (PL) bedded Marcellus shale specimens during constant stress state: **(a)** PD-1, **(b)** PD-2, **(c)** PD-3, **(d)** PL-1, **(e)** PL-2, and **(f)** PL-3.

calculated using Eq. (1) below [23,27]:

$$\beta^2 = \beta_{obs}^2 - \beta_{ins}^2 \quad (1)$$

where the β_{obs} also corresponds to the measured integral breadth from the XRD line profile.

3. Results and discussion

3.1. Permanent strain results

The strain versus time curves for the bedded Marcellus shale specimens during the constant stress state are displayed in Fig. 2. The constantly increasing axial stress caused axial and radial strain in the PD-1 and PL-1, also called as instantaneous strain (Fig. 2(a-d)). Both instantaneous and time-dependent strains in axial and radial directions were observed in the PD-2, PD-3, PL-2 and PL-3 during longer duration of the constant stress state (Fig. 2(b-c-e-f)). Unlike conventional creep curves including transient and steady creep state, these four shale specimens did not exhibit any transient creep phase. When the axial stress became constant, the strain accumulated in the shale specimens at a constant rate, which is called as steady state creep stage. Besides, PL-2 and PL-3 specimens showed an exponential increase in radial strain after a certain period of constant stress state, implying the onset of tertiary creep stage.

After complete removal of the constant stress, the permanent strain in all shale specimens were recorded in axial and radial directions, and these results are summarized in Table 2. The level of the constant stress with respect to the failure strength on Marcellus shale was similar among all parallel (PL) and perpendicular (PD) bedded specimens. Therefore, the total permanent strain (or macrostrain) accumulated in each shale specimen was discussed as a function of the duration of the constant stress state. The results demonstrated that the perpendicular (PD) bedded shale specimens only experienced a permanent strain in the axial direction. However, the permanent strain in both the axial and radial directions was evident in the parallel (PL) bedded shale specimens. Although the level of constant stress was similar (i.e. 70% of short-term strength) for the PL and PD bedded shale specimens, the PL bedded specimens displayed significantly higher permanent strain (radial) compared to the PD bedded ones. The creep experiments on the cubical-shaped specimens of Greenschist in uniaxial and biaxial conditions were also reported.[28] They showed that, at any specific stress level, the creep strain was higher for the parallel bedding orientation compared to the perpendicular bedding orientation. If the orientation of the major principal stress is parallel or sub-parallel to the bedding planes, it was shown that the bedding planes tend to open up.[29] This could explain the higher radial strain in the parallel (PL) bedded Marcellus shale specimens. Among all PD bedded specimens, the PD-3 exhibited the highest permanent axial strain (0.629×10^{-3}) after duration of the constant stress state for 747 h. The permanent axial strain in the PD-1 and PD-2 shale specimens was measured to be 0.414×10^{-3} and 0.191×10^{-3}, respectively. These results clearly showed that the permanent strain accumulated within PD bedded specimens did not show any trend with increasing duration of the constant stress state, even though the axial and confining stress levels were the same. This behavior may be attributed to the structural heterogeneity among the PD bedded shale specimens. In the case of the parallel (PL) bedded shale specimens, the permanent strain in both axial and radial directions increased with increasing duration of the constant stress state as presented in Table 2. The experimental results of uniaxial creep tests on Barre granite specimens similarly showed that total and inelastic strain increased both in axial and radial directions with constant stress.[8] Although the level of increase in the axial strain was highly significant from the PL-1 to PL-2 specimen (0 → 128 h), this increase was found to be very low for the PL-3 specimen after being maintained under the constant stress state for 283 h.

3.2. Bulk mineral identification

All parallel- and perpendicular-bedded Marcellus shale specimens were cut from their top and bottom sides before and after triaxial creep tests, and prepared for the bulk and local chemical analysis or mineral identification. Fig. 3 shows the XRD patterns of the PD and PL bedded shale specimens. The XRD peaks identified at 2θ of 29.4°, 39.4°, 47.5° and 48.5° correspond to the major calcite mineral ($CaCO_3$), and its main diffraction peaks for the (104), (113), (018) and (116) planes, respectively. The presence of the quartz mineral (SiO_2) in the shale specimens was also determined based on the diffraction peaks detected at 2θ of 20.8°, 26.6°, 36.5° and 50.1°, which refer to the (010), (011), (110) and (112) planes, respectively. In addition to the calcite and quartz major phases, the dolomite ($CaMg(CO_3)_2$) and pyrite (FeS_2) minerals were identified as minor phases in the shale specimens. The pyrite mineral peaks were observed at 2θ of 28.5°, 33.0°, 37.1°, 40.8° and 56.3° reflecting the (111), (002), (021), (112) and (113) planes, respectively. The only peak detected at 2θ of 30.8° attributes to the dolomite mineral and its (104) plane.

It is evident that all shale specimens displayed similar XRD patterns and bulk mineralogy only with certain changes in peak intensities and peak shapes. The identification of calcite, quartz, dolomite and pyrite minerals is expected, since the Marcellus shale is typically composed of clay minerals (e.g. illite, illite-smectite, chlorite), quartz, calcite, feldspars and dolomite.[30,31] It is also well known that the concentrations of these minerals vary significantly depending on the collection region and core depth of the shale specimens within the Appalachian Basin.[13,32] In addition, the changes in the peak intensities of the calcite, quartz, pyrite and dolomite minerals for the top- and bottom-sides of the perpendicular (PD) and parallel (PL) bedded shale specimens indicated a certain level of mineralogical heterogeneity in the Marcellus shale. Such intensity changes can be also seen for the top-side and bottom-side cut of the same shale specimens (e.g. PD-1 (B) and PD-1 (T)). These variations in the mineral composition of the Marcellus shale are critical, since their mechanical properties and deformation or microcracking behavior may also vary depending upon the bedding orientation and specific cut location.

3.3. Local mineral identification from non-crack and microcrack areas

In addition to the bulk characterization by XRD, these Marcellus shale specimens were further analyzed by Raman spectroscopy in order

Table 2
Triaxial creep test results of the parallel (PL) and perpendicular (PD) bedded Marcellus shale specimens under constant stress state.

Specimen ID	Specimen type	Confining stress (MPa)	Axial stress (MPa)	Duration of constant stress state (hours)	Permanent Strain (10^{-3})	
					Axial	Radial
PD-1	Perpendicular	6.89	87.66	0	0.414	−0.040
PD-2				209	0.191	0.000
PD-3				747	0.629	0.000
PL-1	Parallel	6.89	95.04	0	0.230	0.000
PL-2				128	0.525	−0.580
PL-3				283	0.561	−2.870

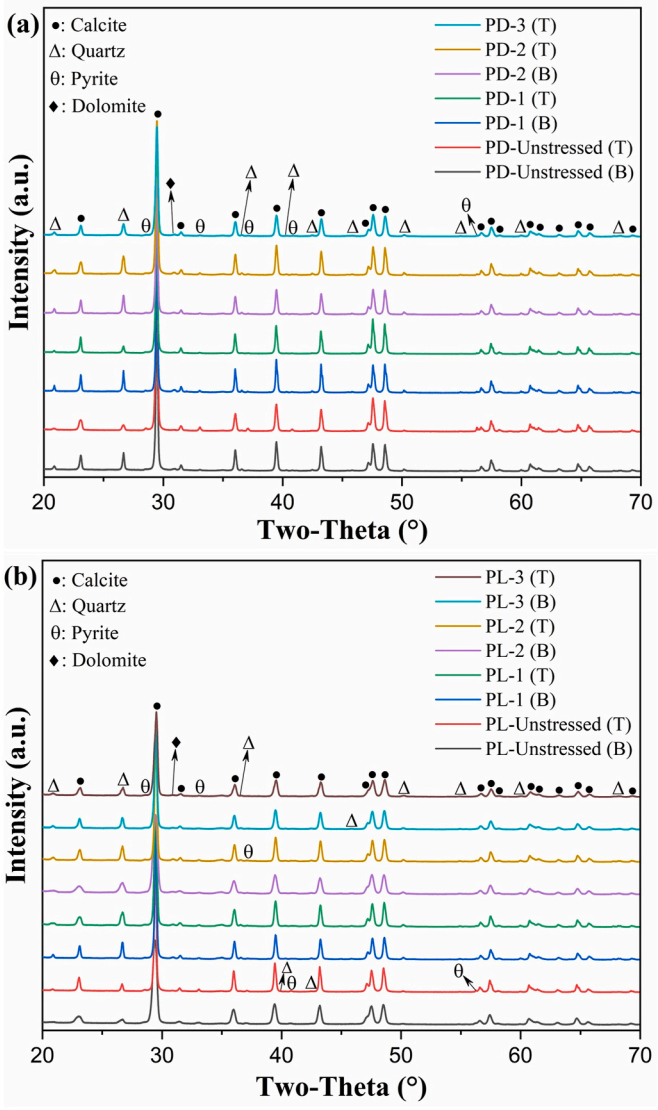

Fig. 3. X-ray diffraction (XRD) patterns of the **(a)** perpendicular (PD) bedded, and **(b)** parallel (PL) bedded Marcellus shale specimens before/after triaxial creep tests.

to examine the local changes in their mineralogy and chemistry within the microcrack and non-crack areas. Prior to the analysis of the shale specimens, the Raman spectra of the standard calcite and quartz powders are shown in Fig. 4(a) as a baseline for a better comparison. The major Raman bands of the baseline calcite mineral were observed at 156, 283, 714 and 1086 cm^{-1}. The most intense and sharp Raman band at 1086 cm^{-1} is attributed to the $\nu_1(CO_3)^{2-}$ symmetric stretching mode.[33] Another characteristic Raman band of the calcite at 714 cm^{-1} refers to ν_4-symmetric $(CO_3)^{2-}$ deformation.[34] The two bands (156 and 283 cm^{-1}) detected in the low Raman shift region of the calcite mineral are often assigned to the external vibrations of the $(CO_3)^{2-}$ group including the rotatory and translatory types of oscillations.[33,35] In addition, two weak Raman bands for the calcite were located at 1437 and 1750 cm^{-1}, which correspond to the ν_3-asymmetric $(CO_3)^{2-}$ stretching mode and the (ν_1 + ν_4) combination band, respectively. For the baseline quartz mineral (Fig. 4(a)), the major Raman bands were detected at 466, 129, 207, while the weak bands were at 265, 356, 400, 510, 697, 808, 1067, 1083 and 1161 cm^{-1}.[36] It is reported that the main fingerprint Raman band of the α-quartz (around 465 cm^{-1}) is attributed to the Si–O–Si symmetric stretching mode.[37,38] The other main peaks of the quartz mineral located at 129 and 207 cm^{-1} are related to the rotation of the SiO_4 tetrahedron and Si–O–Si bond angle inside the SiO_4 tetrahedron (deformational bending vibrational mode), respectively.[39,40]

Following the baseline data, Fig. 4 presents the Raman spectra of the perpendicular (PD) and parallel (PL) bedded shale specimens collected from the non-crack areas (Fig. 4(b–c)) and the microcrack areas (Fig. 4 (d–e)). For both PD and PL bedded shale specimens, the Raman bands detected at around 156, 282, 714 and 1086 cm^{-1} clearly presents the calcite mineral as the major crystalline phase within the non-crack areas (Fig. 4(b–c)). It is evident that the characteristic Raman bands of the calcite mineral are visible for the non-crack areas of all shale specimens. In addition, two distinct broad Raman bands were located at 1355 and 1605 cm^{-1}, which correspond to the characteristic D (disordered) and G (graphitic) bands of carbon, respectively.[16] The Raman band at 1265 cm^{-1} also refers to the shoulder D2 band associated with the amorphous carbon structure.[41] These peaks clearly demonstrated the certain presence of amorphous organic matter within the Marcellus shale specimens. This organic matter is typically known as a kerogen, which is defined as a dispersed carbonaceous residue.[16,42] It can be trapped and observed in various rock specimens (e.g. organic-rich shales, marble, limestone).[30,32,35] Besides, it should be noted that the quartz, dolomite, and pyrite minerals were not detected in their Raman spectra. This indicated their minor concentrations with respect to the major calcite phase, which is in good agreement with the XRD results.

When the Raman data was further collected from the microcrack areas from the same PD and PL bedded shale specimens, significant changes were observed (Fig. 4(d–e)). The Raman bands of the calcite mineral at 156, 282 and 714 cm^{-1} almost completely disappeared. In addition, the intensity of its major Raman band at 1086 cm^{-1} significantly reduced, and this band was not observed for some of the shale specimens (e.g. PD-1 (B), PD-2 (T), PL-1 (T)) in the microcrack area. On the other hand, no significant changes were observed on the Raman bands of the organic matter or kerogen. Lastly, two additional Raman bands were detected at around 340 and 378 cm^{-1} only for the PD-Unstressed (T) specimen, which may be attributed to the quartz mineral. These results clearly demonstrated that the concentrations of the calcite and organic matter highly varied in the non-crack and microcrack areas. The microcrack areas existing in the PD and PL bedded shale specimens were found to be organic-rich. This clearly implies that the microcracking and deformation behavior of the Marcellus shale specimens are highly influenced by the presence of organic matter and its concentration.

3.4. Residual strain within the shale specimens

It is known that the changes in the XRD line profiles can be efficiently used to estimate the residual strain in the materials. Therefore, the major peaks of each mineral within the perpendicular (PD) and parallel (PL) bedded shale specimens are shown in Fig. 5(a,d). In addition, the focused view of the major peaks of the calcite and quartz minerals (major phases) are presented in Fig. 5(b,c,e,f). The characteristic major peak positions of calcite ($2\theta = 29.41°$) and quartz ($2\theta = 26.63°$) minerals are also shown with dashed lines for a better comparison. In a polycrystalline specimen, a certain shift in the peak position occurs due to the changes in a plane spacing induced by a uniform (homogeneous) compressive or tensile strain in all crystal grains.[23] Therefore, the observation of any peak shift in the XRD pattern typically implies the presence of a macrostrain.[43,44] For most of the PD and PL bedded shale specimens, slight positive peak shifts by 0.03–0.05° with respect to the reference calcite and quartz peaks were observed (Fig. 5(b and c)). This indicated the existence of a certain level of compressive macrostrain in the PD shale specimens.[45] Similarly, positive peak shifts (by 0.02–0.11°) can be seen for the PL bedded shale specimens. However, it is evident that the peak shifts were more significant, implying relatively higher level of compressive macrostrain in the PL specimens. Slight peak shifts were also observed for the unstressed PD and PL bedded shale specimens, indicating the pre-existing macrostrain. On the other hand, no

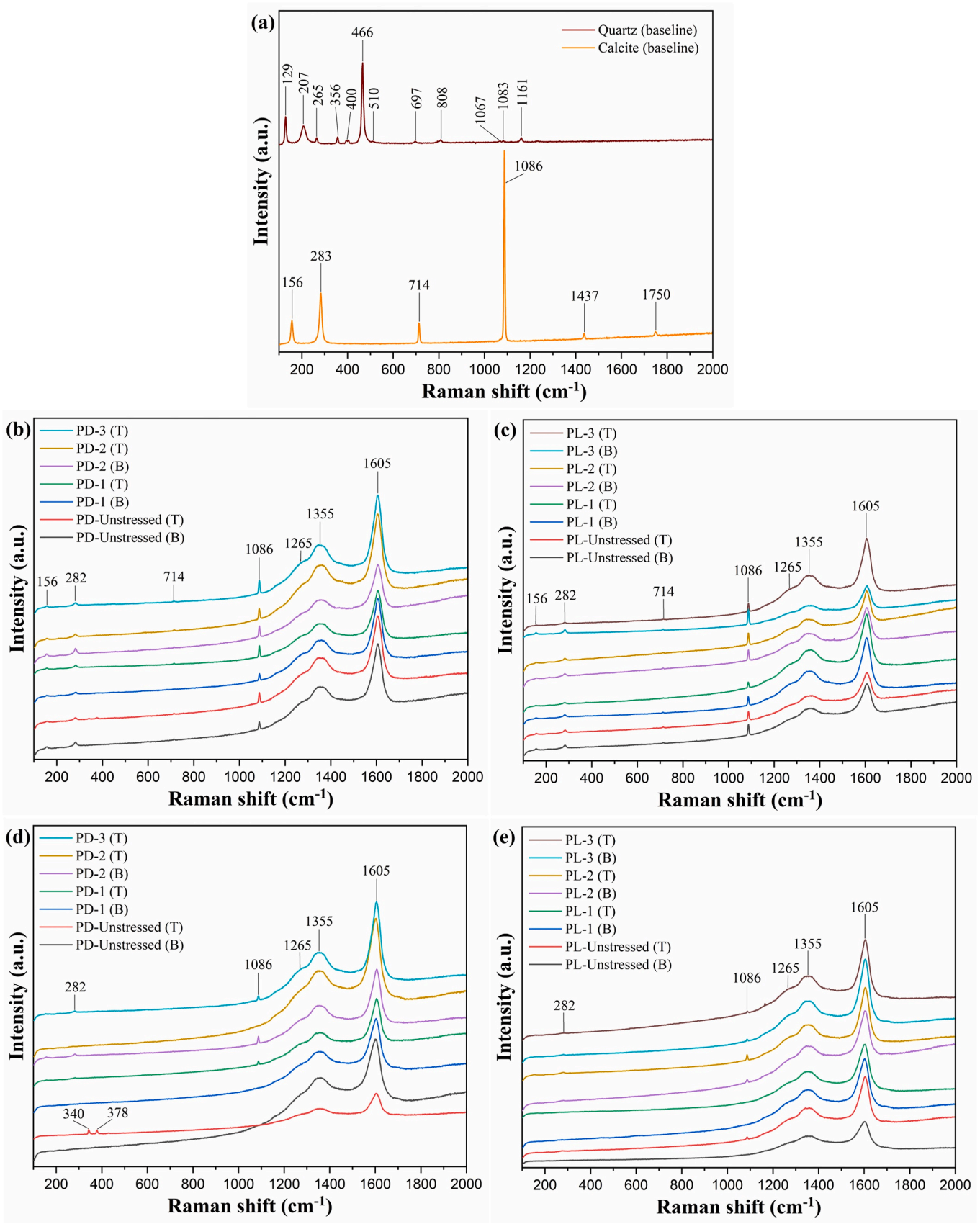

Fig. 4. Raman spectra of the **(a)** standard calcite and quartz powders (baseline), and the perpendicular (PD) and parallel (PL) bedded Marcellus shale specimens from their **(b–c)** non-crack areas, and **(d–e)** microcrack areas, before/after triaxial creep tests.

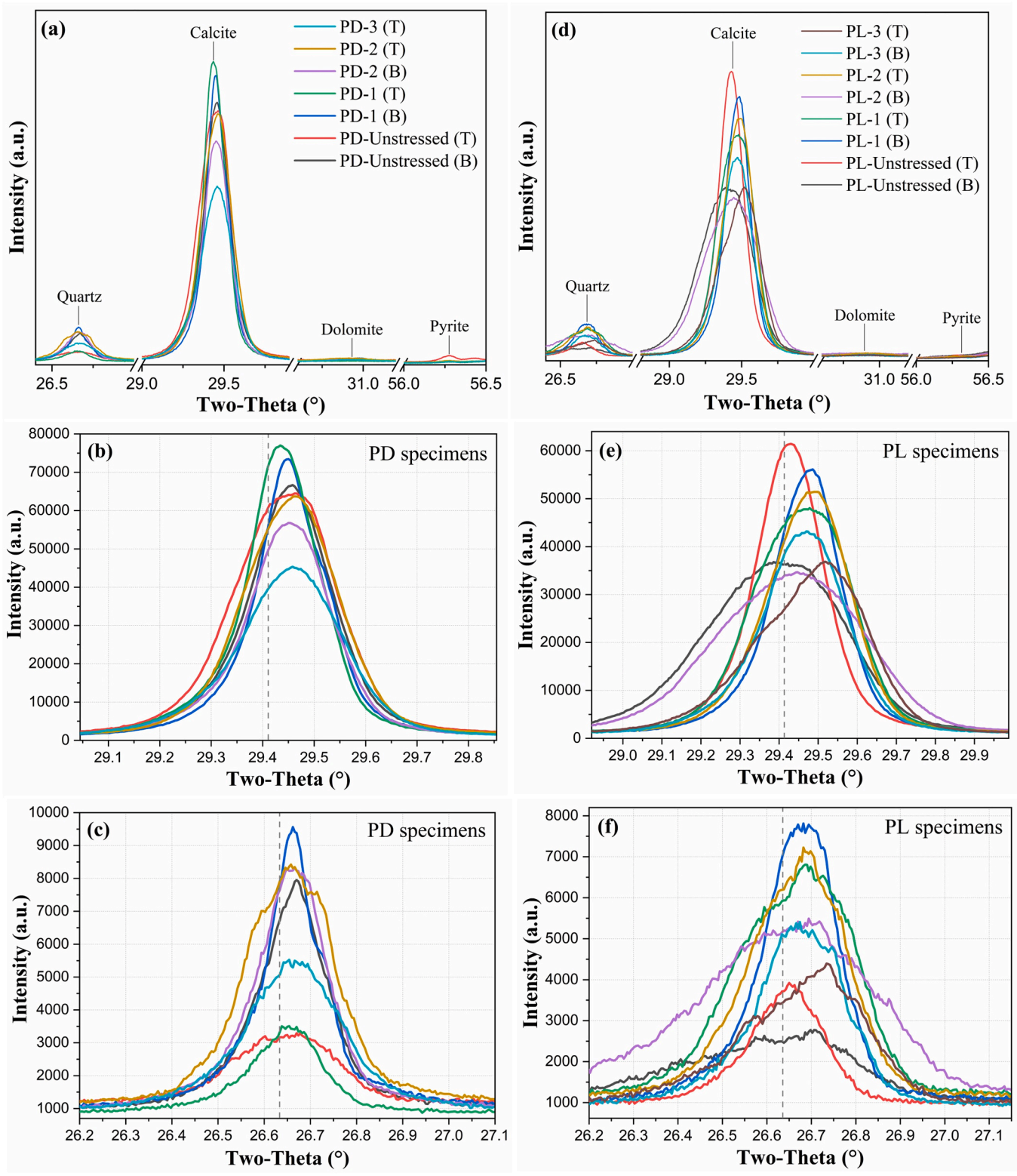

Fig. 5. **(a,d)** Major XRD peaks of each mineral, and focused view of the major XRD peaks of **(b,e)** calcite and **(c,f)** quartz, for the perpendicular (PD) and parallel (PL) bedded Marcellus shale specimens before/after triaxial creep tests.

significant changes in the peak positions were detected for the PD specimens before and after triaxial creep tests. These changes were found to be more significant for the PL specimens. In addition, the level of peak shifts relatively increased for the PL-2 and PL-3 specimens. This clearly indicated that the degree of macrostrain increased after triaxial creep tests, particularly with increasing duration of constant stress state. This is in good agreement with the increased permanent strain in the radial direction for these specimens (as presented in Table 2).

The observation of the macrostrain is important to understand the deformation behavior over a macroscopic scale. However, the mechanical performance and deformation behavior of the materials are mostly controlled by the presence of defects and resultant

microstrains.[11] When a non-uniform (inhomogeneous) strain or commonly termed as microstrain (or lattice strain) is present, distortions in the XRD peak shapes (peak width and height) typically occur.[23,43,46] It is known that both grain size and microstrain effects contribute to these changes in the XRD peak profiles. In this study, to estimate the residual microstrain in the calcite and quartz phases of the shale specimens, the Williamson-Hall method was utilized as described in Eq. (2) below [23,47,48]:

$$\beta \cdot \cos(\theta) = \frac{\lambda}{D} + 4\varepsilon \cdot \sin(\theta) \tag{2}$$

where β is the sample related integral breadth (peak area divided by peak height), θ is the Bragg angle, λ is the wavelength, D is the crystallite size, and ε is the measure of the microstrain. When the size broadening effect (D) is assumed to be negligible for the shale specimens, the slope of a linear fit (with zero intercept) for the plot of $\beta \cdot cos(\theta)$ versus $sin(\theta)$ represents the maximum internal lattice microstrain value (4ε). The Williamson-Hall plots for the individual calcite and quartz minerals are presented in Figs. 6 and 7 for the perpendicular (PD) and parallel (PL) bedded shale specimens, respectively. The microstrain in the calcite and quartz minerals of the PD and PL bedded shale specimens were calculated using the presented Williamson-Hall plots and the slopes of the linear fits. The estimated microstrain values in the calcite and quartz minerals for each shale specimen are listed in Table 3. The average microstrain values in the calcite and quartz minerals are also given in Table 3 as calculated from the top- and bottom-cut of the same shale specimen. It should be noted that the microstrain in the pyrite and dolomite minerals as minor phases were not calculated due to very limited number of low-intensity XRD peaks detected.

The results showed that the microstrain levels in both calcite and quartz varied for the top- and bottom-cut of all PD and PL bedded shale specimens. This may be directly correlated to the mineralogical heterogeneity within the Marcellus shale specimens, as similarly identified by the XRD studies (e.g. peak intensity variations). On the basis of this fact, the average microstrain levels were used for further discussion. The presence of a certain level of pre-existing microstrain was detected prior to the triaxial creep tests (unstressed specimens). The microstrain levels in calcite and quartz were similar (5.85-6.05 $\times$ 10^{-3}) for the PD-Unstressed specimen. Similar level of microstrain in quartz (6.05 $\times$ 10^{-3}) was also detected for the PL-Unstressed specimen. However, it is

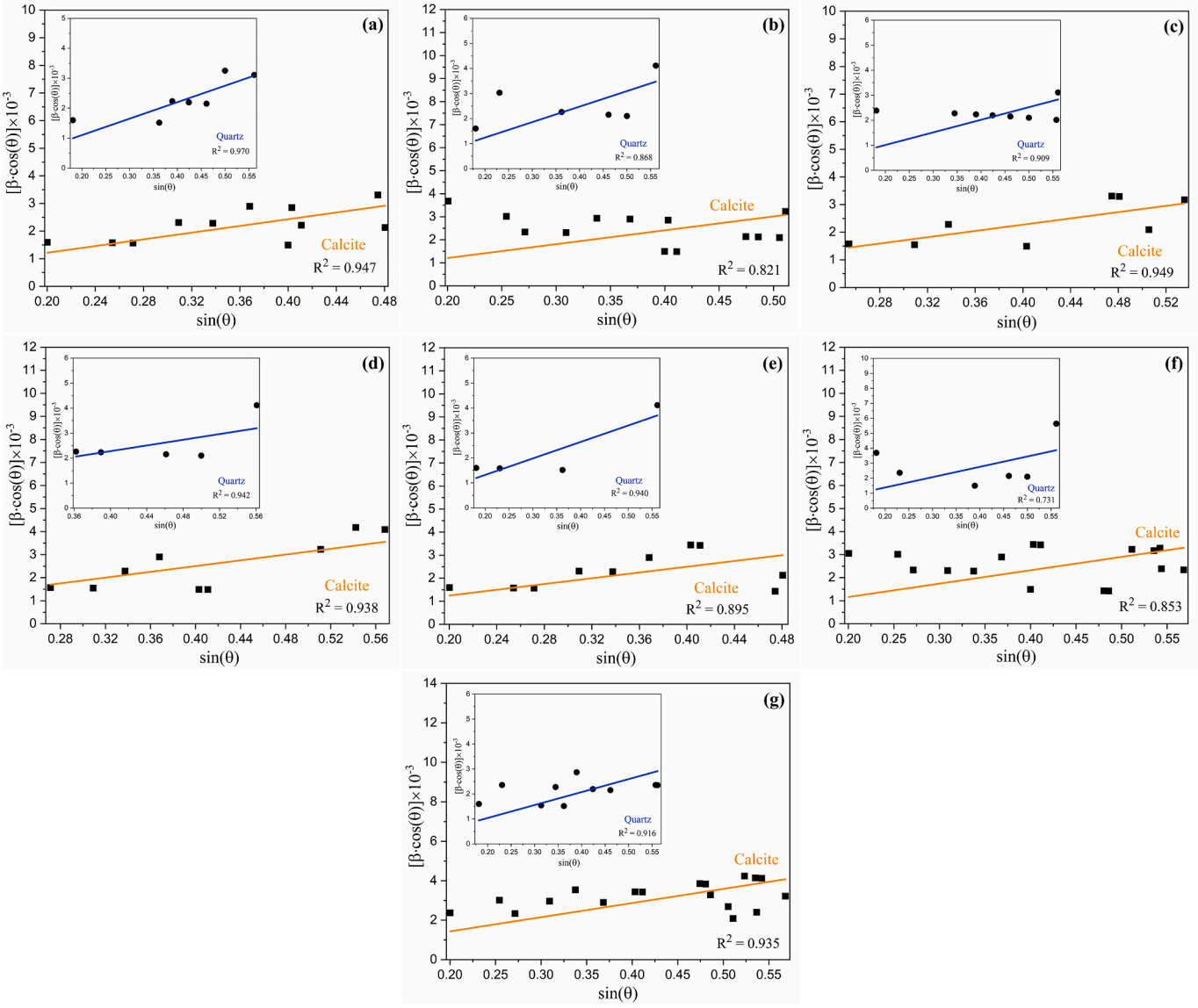

Fig. 6. Williamson-Hall plots for the calcite and quartz minerals of the perpendicular (PD) bedded Marcellus shale specimens before/after triaxial creep tests: **(a)** PD-Unstressed (B), **(b)** PD-Unstressed (T), **(c)** PD-1 (B), **(d)** PD-1 (T), **(e)** PD-2 (B), **(f)** PD-2 (T), and **(g)** PD-3 (T).

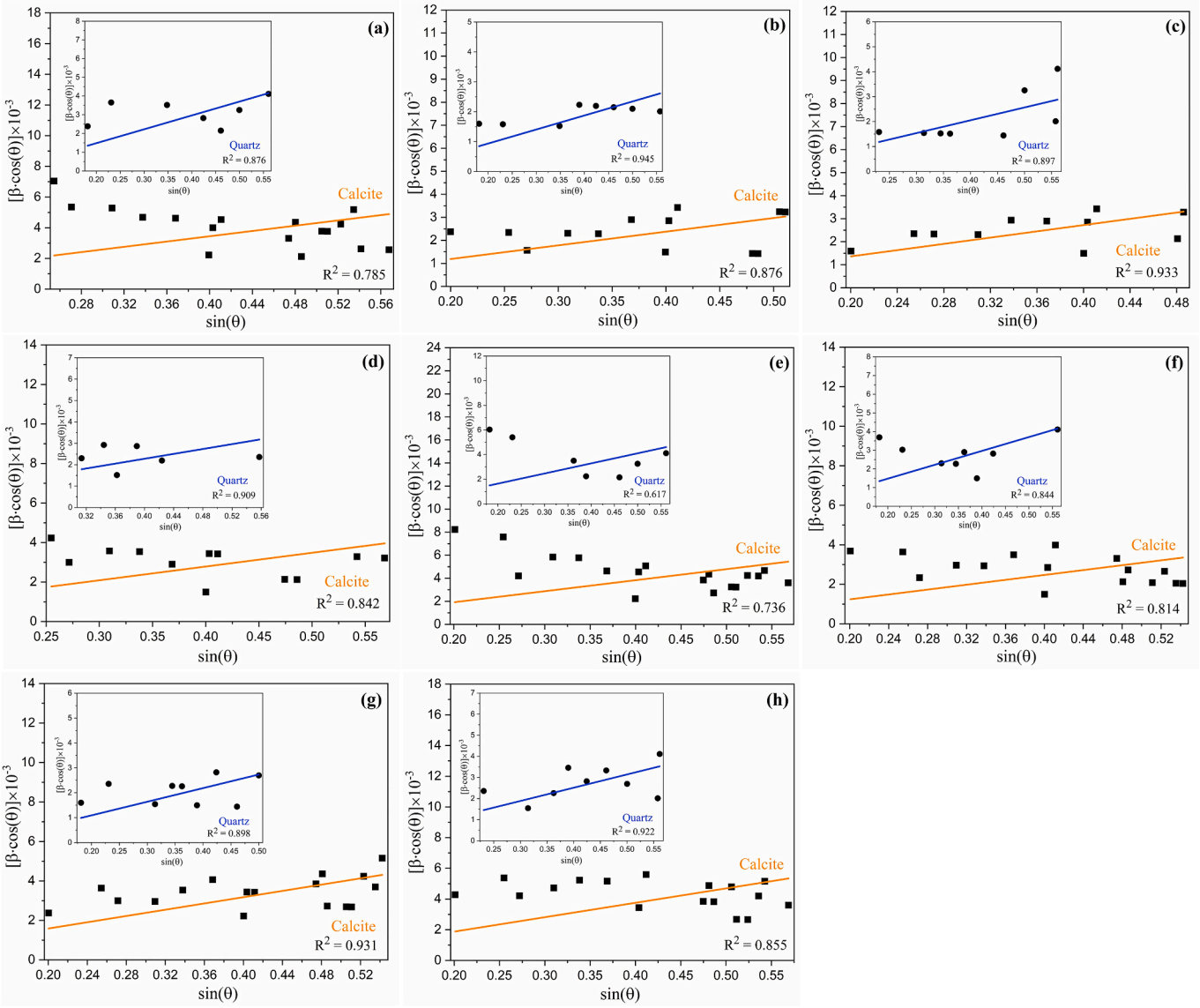

Fig. 7. Williamson-Hall plots for the calcite and quartz minerals of the parallel (PL) bedded Marcellus shale specimens before/after triaxial creep tests: **(a)** PL-Unstressed (B), **(b)** PL-Unstressed (T), **(c)** PL-1 (B), **(d)** PL-1 (T), **(e)** PL-2 (B), **(f)** PL-2 (T), **(g)** PL-3 (B), and **(h)** PL-3 (T).

evident that the calcite displayed higher amount of microstrain (7.27×10^{-3}) for the PL-Unstressed specimen. These results indicated the higher concentration of pre-existing dislocations and/or other lattice defects (e.g. point defect, stacking, twin fault), and associated microstrain within the calcite grains of the parallel (PL) bedded unstressed shale specimen. This also confirms the anisotropic nature of Marcellus shales due to bedding.[49]

After triaxial creep tests, significant changes in the average microstrain within the calcite and quartz phases were detected for all shale specimens. For the perpendicular (PD) bedded shale specimens, the microstrain in the calcite mineral almost did not change after being maintained under constant stress state for 208.8 h (PD-2). With further increase in the duration of the constant stress state to 746.8 h (PD-3), the microstrain in calcite increased from 6.02×10^{-3} to 7.17×10^{-3}. In the case of the quartz phase of the PD bedded shale specimens, highest microstrain (6.75×10^{-3}) was observed for the PD-2. Following this, the microstrain in quartz phase decreased to 5.19×10^{-3} with increasing duration of constant stress state (PD-3). This may indicate the existence of a strain recovery mechanism in quartz phase, which needs to be further studied. For the parallel (PL) bedded shale specimens, similar trends in the average microstrain levels were identified. The microstrain in calcite phase of the PL-1 was similar to the unstressed one. However, it increased significantly from 6.88×10^{-3} (PL-1) to 8.66×10^{-3} (PL-3) with increasing duration of the constant stress state. Similar to the trends in the PD bedded shale specimens, the highest microstrain (7.81×10^{-3}) in the quartz phase for the PL samples was detected for the PL-2 after being maintained under constant stress state for 128.2 h. Furthermore, their permanent strain (or macrostrain) and average microstrain are summarized in Table 4. No significant correlation was observed between macrostrain and microstrain data, except for the PL specimens. It can be seen that both average microstrain in the calcite phase and total macrostrain increased for the PL specimens after longer duration of the constant stress state.

In summary, it is evident that the microstrain levels in calcite phase were higher than that in the quartz phase for all shale specimens (except for the PD-2). This is due to the formation of more lattice defects, and thereby, increased microstrain-induced deformation in the calcite phase of the Marcellus shale, particularly compared to the quartz phase. It is known that there are many parameters affecting the mechanical strength and elasticity of shales (e.g. total clay/kerogen content, porosity), but it is mainly dictated by their mineralogical composition.[49,50] While quartz and pyrite are known as strong phases, the

Table 3
Microstrain (ε) in the calcite and quartz minerals for the perpendicular (PD) and parallel (PL) bedded Marcellus shale specimens before/after triaxial creep tests, estimated using the Williamson-Hall plots.

Shale specimen ID	Microstrain ($\varepsilon \times 10^{-3}$)	
	CALCITE	QUARTZ
PD-Unstressed (B)	6.075 (±0.433)	5.501 (±0.365)
PD-Unstressed (T)	6.025 (±0.775)	6.191 (±0.972)
Average	6.050	5.846
PD-1 (B)	5.681 (±0.462)	5.043 (±0.560)
PD-1 (T)	6.256 (±0.533)	5.695 (±0.626)
Average	5.969	5.369
PD-2 (B)	6.245 (±0.673)	6.601 (±0.830)
PD-2 (T)	5.803 (±0.599)	6.900 (±1.659)
Average	6.024	6.751
PD-3 (T)	7.171 (±0.444)	5.191 (±0.495)
PL-Unstressed (B)	8.609 (±1.084)	7.411 (±1.046)
PL-Unstressed (T)	5.939 (±0.618)	4.688 (±0.398)
Average	7.272	6.050
PL-1 (B)	6.801 (±0.550)	5.132 (±0.612)
PL-1 (T)	6.958 (±0.865)	5.697 (±0.728)
Average	6.880	5.415
PL-2 (B)	9.572 (±1.339)	8.210 (±2.342)
PL-2 (T)	6.174 (±0.734)	7.413 (±1.114)
Average	7.873	7.812
PL-3 (B)	7.942 (±0.523)	5.467 (±0.609)
PL-3 (T)	9.385 (±0.933)	6.284 (±0.606)
Average	8.664	5.876

* The numbers given in parenthesis represents the standard error in microstrain (ε).
* Microstrain values have no unit.

Table 4
Summary of the permanent strain (or macrostrain) in axial/radial direction and average microstrain (ε) data for the perpendicular (PD) and parallel (PL) bedded Marcellus shale specimens after the triaxial creep tests.

Specimen ID	Permanent Strain or Macrostrain (10^{-3})		Average Microstrain ($\varepsilon \times 10^{-3}$)	
	Axial	Radial	Calcite	Quartz
PD-1	0.414	−0.040	5.969	5.369
PD-2	0.191	0.000	6.024	6.751
PD-3	0.629	0.000	7.171	5.191
PL-1	0.230	0.000	6.880	5.415
PL-2	0.525	−0.580	7.873	7.812
PL-3	0.561	−2.870	8.664	5.876

carbonates (e.g. calcite) are typically considered as intermediate strong minerals. In addition, clays and kerogen are the weakest phases within the shale structure. The more microstrain and deformation identified in the calcite phase of the Marcellus shale specimens can be explained on the basis of this fact. Therefore, the lower microstrain and deformation was determined in the quartz phase. In comparison of the PD and PL bedded shale specimens, it can be stated that higher amount of microstrain in both calcite and quartz phases were observed for the PL bedding orientation. The good correlation between high permanent radial strain and high microstrain (lattice strain) is also evident for the PL bedded shale specimens. The identification of the higher level of inhomogeneous microstrain in the calcite phase, and also in the shale specimens cored parallel to the bedding orientation, is critical for a mechanistic understanding at the micron scale. This could lead to the initiation of more microcracks in the calcite phase (compared to quartz), since it is known that the initiation of the microcracks are mostly interrelated with inhomogeneous strain concentration in the grains under creep or fatigue conditions.[51] This indicated that microcracking and associated deformation of the Marcellus shale progressed mainly with the higher level of microstrain generated in the calcite mineral under triaxial creep conditions.

4. Conclusions

For a better fundamental understanding on microcracking and deformation behavior, the Marcellus shale specimens cored parallel and perpendicular to the bedding orientation were characterized by XRD and Raman spectroscopy. The Williamson-Hall method before/after triaxial creep tests under constant stress was used to estimate the level of microstrain within the major phases. The parallel-bedded shales experienced higher permanent strain in radial direction, which also increased with increasing duration of the constant stress state. It also confirmed the anisotropic nature of the shales due to bedding. The XRD studies showed their mineralogy including calcite, quartz, pyrite and dolomite phases, and indicated a certain level of mineralogical heterogeneity. The local mineral identification studies showed the presence of an organic matter (kerogen) both in non-crack and microcrack areas. The data collected from the microcrack areas implied that the microcracking in shales are highly influenced by organic matter and its concentration. The XRD peak shifts indicated the pre-existing macrostrain, which increased after long-term triaxial creep tests. Besides, changes in the peak shapes and associated microstrain levels were analyzed using the Williamson-Hall method. The amount of microstrain was found to be much higher in the calcite compared to the quartz phase, indicating the presence of more lattice defects. The parallel-bedded shales also displayed higher microstrain compared to the perpendicular ones. This knowledge is crucial, since the high level of inhomogeneous lattice strain (microstrain) could lead to the initiation of more microcracks in the calcite. In conclusion, these results clearly showed that the microcracking and associated mechanical deformation of the Marcellus shale was mainly dictated by presence of organic matter, concentration of lattice defects and associated microstrain in calcite (partially quartz), and bedding orientation.

Acknowledgments

This research was supported by the U.S. National Institute for Occupational Safety and Health (NIOSH) under contract no. 200-2016-92214. We acknowledge the use of the West Virginia University Shared Research Facilities (WVU-SRF). We also greatly appreciate the assistance of Dr. Qiang Wang (WVU-SRF) on X-ray diffraction experiments.

References

1 Gupta N. *Fundamental Mechanism of Time-dependent Failure in Shale*. Morgantown WV, USA: West Virginia University; 2019.
2 Ruppert L, Tewalt S, Bragg L, Wallack R. A digital resource model of the upper Pennsylvanian Pittsburgh coal bed, Monongahela Group, northern Appalachian basin coal region, USA. *Int J Coal Geol*. 1999;41(1-2):3–24.
3 Molinda GM, Mark C. *Rating the Strength of Coal Mine Roof Rocks*. vol. 9444. United States Department of the Interior, Bureau of Mines; 1996.
4 Molinda GM, Oyler DC, Gurgenli H. Identifying moisture sensitive roof rocks in coal mines. In: *25th International Conference on Ground Control in Mining*. USA: Morgantown WV; 2006:57–64.
5 Griggs D. Creep of rocks. *J Geol*. 1939;47(3):225–251.
6 Sone H. *Mechanical Properties of Shale Gas Reservoir Rocks and its Relation to the In-Situ Stress Variation Observed in Shale Gas Reservoirs*. Stanford CA, USA: Stanford University; 2012.
7 Khosravi E. *An Experimental Investigation on Creep Behavior of Shale Rocks: With Emphasis on the Influence of Temperature and Anisotropy*. Norman OK, USA: University of Oklahoma; 2017.
8 Kranz RL. Crack growth and development during creep of barre granite. *Int J Rock Mech Min Sci*. 1979;16(1):23–35.
9 Martin RJ. Time-dependent crack growth in quartz and its application to creep of rocks. *J Geophys Res*. 1972;77(8):1406.
10 Sang G, Liu S, Zhang R, Elsworth D, He L. Nanopore characterization of mine roof shales by SANS, nitrogen adsorption, and mercury intrusion: impact on water adsorption/retention behavior. *Int J Coal Geol*. 2018;200:173–185.
11 Dobrosz P, Bull S, Olsen S, et al. Measurement of the residual macro and microstrain in strained Si/SiGe using Raman spectroscopy. In: *High-Mobility Group-Iv Materials and Devices*. 809. 2004:109–114.
12 Ciobota V, Salama W, Jentzsch P, et al. Raman investigations of upper cretaceous phosphorite and black shale from Safaga District, Red Sea, Egypt. *Spectrochim Acta Mol Biomol Spectrosc*. 2014;118:42–47.

13 Hupp B, Donovan J. Quantitative mineralogy for facies definition in the Marcellus Shale (Appalachian Basin, USA) using XRD-XRF integration. *Sediment Geol*. 2018; 371:16–31.
14 Duee C, Orberger B, Maubec N, et al. Impact of heterogeneities and surface roughness on pXRF, pIR, XRD and Raman analyses: challenges for on-line, real-time combined mineralogical and chemical analyses on drill cores and implication for "high speed" Ni-laterite exploration. *J Geochem Explor*. 2019;198:1–17.
15 Chen M, Zhu J, Zhan H, et al. Direct detection of oil shale yields: a laser-induced voltage investigation. *Energy Fuels*. 2019;33(2):1069–1073.
16 Tuschel D. Raman spectroscopy of oil shale. *Spectroscopy*. 2013;28(3):20–27.
17 Chittan M, Kumar C, Sowjanya K, Kumar B. Estimation of lattice strain in nanometer-sized alumina doped ZnO ceramics by X-ray peak profile Analysis. *Mater Today-Proceedings*. 2017;4(8):9237–9245.
18 Deb A, Chatterjee P. Estimation of lattice strain in alumina-zirconia nanocomposites by X-ray diffraction peak profile analysis. *J Theor Appl Phys*. 2019;13(3):221–229.
19 Mote VD, Purushotham Y, Dole BN. Williamson-Hall analysis in estimation of lattice strain in nanometer-sized ZnO particles. *J Theor Appl Phys*. 2012;6(6).
20 Williamson GK, Hall WH. X-ray line broadening from filed aluminium and wolfram. *Acta Metall*. 1953;1(1):22–31.
21 Roen JB. Geology of the devonian black shales of the Appalachian Basin. *Org Geochem*. 1984;5(4):241–254.
22 ASTM. *D7012-14e1 Standard test methods for compressive strength and elastic moduli of intact rock core specimens under varying states of stress and temperatures*. West Conshohocken, PA: ASTM International; 2014.
23 Waseda Y, Matsubara E, Shinoda K. *X-Ray Diffraction Crystallography: Introduction, Examples and Solved Problems*. Berlin Heidelberg: Springer-Verlag; 2011.
24 Scardi P, Leoni M, Bertamini L. Influence of phase stability on the residual stress in partially stabilized zirconia TBC produced by plasma spray. *Surf Coating Technol*. 1995;76(1-3):106–112.
25 Scardi P. *X-ray Diffraction from Thin Films: Size/strain Analysis and Whole Pattern Fitting*. Italy: Istituto Nazionale di Fisica Nucleare: Frascati; 1996:85–112.
26 Scardi P, Lutterotti L, Maistrelli P. Experimental determination of the instrumental broadening in the Bragg-Brentano geometry. *Powder Diffr*. 1994;9(3):180–186.
27 Prabhu YT, Rao KV, Kumar VSS, Kumari BS. X-ray analysis by Williamson-Hall and Size-Strain plot methods of ZnO nanoparticles with fuel variation. *World J Nano Sci Eng*. 2014;4:21–28.
28 Wu C, Chen Q, Basack S, Xu R, Shi Z. Biaxial creep test study on the influence of structural anisotropy on rheological behavior of hard rock. *J Mater Civ Eng*. 2016;28 (10).
29 Zhang C-L, Armand G, Conil N, Laurich B. Investigation on anisotropy of mechanical properties of Callovo-Oxfordian claystone. *Eng Geol*. 2019;251:128–145.
30 Vankeuren A, Hakala J, Jarvis K, Moore J. Mineral reactions in shale gas reservoirs: barite scale formation from reusing produced water as hydraulic fracturing fluid. *Environ Sci Technol*. 2017;51(16):9391–9402.
31 Emmanuel OO. *Geologic Characterization and the Recognition of Cyclicity in the Middle Devonian Marcellus Shale, Appalachian Basin*. Golden CO, USA: Colorado School of Mines; 2013. NE USA.
32 Wang G, Carr T. Organic-rich Marcellus Shale lithofacies modeling and distribution pattern analysis in the Appalachian Basin. *AAPG Bull*. 2013;97(12):2173–2205.
33 Sun J, Wu Z, Cheng H, Zhang Z, Frost RL. A Raman spectroscopic comparison of calcite and dolomite. *Spectrochim Acta Mol Biomol Spectrosc*. 2014;117:158–162.
34 Gunasekaran S, Anbalagan G, Pandi S. Raman and infrared spectra of carbonates of calcite structure. *J Raman Spectrosc*. 2006;37:892–899.
35 Khrissi S, Haddad M, Bejjit L, et al. Raman and XRD characterization of Moroccan marbles. *Xii Maghreb Days of material sciences. IOP Conf SerMater Sci Eng*. 2017:186.
36 Kotnala R, Gupta R, Shukla A, Jain S, Gaur A, Shah J. Metal oxide based hydroelectric cell for electricity generation by water molecule dissociation without electrolyte/acid. *J Phys Chem C*. 2018;122(33):18841–18849.
37 Enami M, Nishtyama T, Mouri T. Laser Raman microspectrometry of metamorphic quartz: a simple method for comparison of metamorphic pressures. *Am Mineral*. 2007;92(8-9):1303–1315.
38 Sharma S, Porter J, Misra A, Acosta-Maeda T, Singh U, Sugimoto N. Multiwavelength scanning standoff time-resolved Raman system for planetary exploration and environmental monitoring. In: *Lidar Remote Sensing For Environmental Monitoring Xvi*. 2018:10779.
39 Skulteti A, Toth T, Fintor K, Schubert F. Deformation history reconstruction using single quartz grain Raman microspectroscopy data. *J Raman Spectrosc*. 2014;45(4): 314–321.
40 Etchepare J, Merian M, Smetankine L. Vibrational normal modes of SiO_2. 1. Alpha and beta quartz. *J Chem Phys*. 1974;60(5):1873–1876.
41 Oschatz M, Boukhalfa S, Nickel W, et al. Kroll-carbons based on silica and alumina templates as high-rate electrode materials in electrochemical double-layer capacitors. *J Mater Chem*. 2014;2(14):5131–5139.
42 Jehlicka J, St'astna A, Prikryl R. Raman spectral characterization of dispersed carbonaceous matter in decorative crystalline limestones. *Spectrochim Acta Mol Biomol Spectrosc*. 2009;73(3):404–409.
43 Jeyaprakash B, Kesavan K, Kumar R, Mohan S, Amalarani A. Temperature dependent grain-size and microstrain of CdO thin films prepared by spray pyrolysis method. *Bull Mater Sci*. 2011;34(4):601–605.
44 Sciti D, Celotti G, Pezzotti G, Guicciardi S. On the toughening mechanisms of $MoSi_2$ reinforced Si_3N_4 ceramics. *Appl Phys Mater Sci Process*. 2007;86(2):243–248.
45 Safeen K, Micheli V, Bartali R, Gottardi G, Laidani N. Low temperature growth study of nano-crystalline TiO_2 thin films deposited by RF sputtering. *J Phys D Appl Phys*. 2015;48(29).
46 Aboud A, Mukherjee A, Revaprasadu N, Mohamed A. The effect of Cu-doping on CdS thin films deposited by the spray pyrolysis technique. *J Mater Res Technol*. 2019;8(2): 2021–2030.
47 Thandavan T, Gani S, Wong C, Nor R. Evaluation of Williamson-Hall strain and stress distribution in ZnO nanowires prepared using aliphatic alcohol. *J Nondestr Eval*. 2015;34(2).
48 Goncalves N, Carvalho J, Lima Z, Sasaki J. Size-strain study of NiO nanoparticles by X-ray powder diffraction line broadening. *Mater Lett*. 2012;72:36–38.
49 Rybacki E, Reinicke A, Meier T, Makasi M, Dresen G. What controls the mechanical properties of shale rocks? - Part I: strength and Young's modulus. *J Petrol Sci Eng*. 2015;135:702–722.
50 Rybacki E, Meier T, Dresen G. What controls the mechanical properties of shale rocks? - Part II: Brittleness. *J Petrol Sci Eng*. 2016;144:39–58.
51 Arai M, Ogata T, Nitta A. Microcrack initiation and propagation mechanism based on microstrain distribution analysis under creep-fatigue condition. *Trans Eng Sci*. 1996; 13.